Soft Matter

PAPER

Cite this: *Soft Matter*, 2019, **15**, 9520

Depletion-driven morphological transitions in hexagonal crystallites of virus rods†

Baeckkyoung Sung, [a] Henricus Herman Wensink [b] and Eric Grelet *[a]

Received 17th June 2019,
Accepted 28th October 2019

DOI: 10.1039/c9sm01207a

rsc.li/soft-matter-journal

The assembly of nanometer-sized building blocks into complex morphologies is not only of fundamental interest but also plays a key role in material science and nanotechnology. We show that the shape of self-assembled superstructures formed by rod-like viruses can be controlled by tuning the attraction *via* the depletion interaction between the rods. Using non-adsorbing polymers as a depleting agent, we demonstrate that a hierarchical unidimensional self-organization into crystalline clusters emerges progressively upon increasing depletion attraction and enhanced growth kinetics. We observe a polymorphic change proceeding from two-dimensional (2D) crystalline monolayers at weak depletion to one-dimensional (1D) columnar fibers at strong depletion, *via* the formation of smectic fibrils at intermediate depletion strength. A simple theory for reversible polymerization enables us to determine the typical bond energy between monomeric units making up the smectic fibrils. We also demonstrate that gentle flow-assistance can be used to template filament-like structures into highly aligned supported films. Our results showcase a generic bottom-up approach for tuning the morphology of crystalline superstructures through modification of the interaction between non-spherical building blocks. This provides a convenient pathway for controlling self-organization, dimensionality and structure-formation of anisotropic nanoparticles for use in nanotechnology and functional materials.

Introduction

The ability to control the shape and symmetry of structures formed through self-assembly processes is of fundamental importance in fabricating highly-ordered nano- and micro-structures.[1,2] The large diversity of morphologies emerging from such superstructures finds applications in photonics,[3–5] electronics,[6,7] sustainable energy,[8–10] drug delivery[11,12] and bioengineering.[13,14] Finding ways to guide nanoparticle self-assembly into mono- and multi-layer structures, bundles, tubes, spherical or polyhedral shells, and more complex geometries has been one of the most pursued research themes in nanoscience. One of the main driving forces for studying controlled nanoparticle self-assembly is the many applications in nanotechnology ranging from tunable optical properties,[15,16] anisotropic electron transport,[17,18] to functional surface topography.[19,20] Among such complex architectures, unidimensional (1D) fibers and bidimensional (2D) superlattices composed of rod-shaped building blocks are of particular interest in view of their intrinsic anisotropic properties. For example, fibers of 1D aligned carbon nanotubes, obtained from various spinning techniques, exhibit high mechanical stiffness and outstanding electrical performance.[21–23] Moreover, 2D long-ranged crystalline monolayers of inorganic nanorods, obtained usually by template or catalyst driven growth, can be used for generating surface plasmonics or piezoelectricity, or for creating photonic crystals.[24–27]

Contrary to spherical nanoparticles, reports on controlled self-assembly of rod-shaped particles are scarce, and no clear indications of polymorphisms in their self-assembled structures have been adequately demonstrated so far. In view of this, we address the following two questions. First, what variety of ordered anisotropic superstructures can be expected if we were able to systematically tune the interparticle forces in a colloidal suspension of rods? And more specifically, is it possible to define a pathway enabling us to control the shape of these self-assembled objects from predominantly unidimensional (fiber-like) to bidimensional (disk-shaped) without compromising their long-range crystalline order? For this purpose, the depletion interaction[28] appears to be a suitable and versatile mechanism for controlling particle interaction, as the range and strength of depletion interaction are determined by the polymer size and concentration, respectively.[29] We will show that introducing tunable depletion interactions with a suitable range indeed leads to a high degree of controlled self-assembly generating a wide variety of crystallite morphologies without the need to use microscale confinements[30] or interfacial effects.[31,32]

---

[a] *Centre de Recherche Paul Pascal, UMR 5031, CNRS & Université de Bordeaux, 33600 Pessac, France. E-mail: eric.grelet@crpp.cnrs.fr*

[b] *Laboratoire de Physique des Solides, UMR 8502, CNRS & Université Paris-Sud, Université Paris-Saclay, 91405 Orsay, France*

† Electronic supplementary information (ESI) available. See DOI: 10.1039/c9sm01207a

It is well known that adding non-adsorbing polymers to colloidal suspension provides an efficient method to induce effective particle–particle attraction that can direct hierarchical organization processes.[33–39] Experimental and theoretical studies on model systems of rod-like particles such as fd viruses have established that the experimental conditions are such that the formation of partially-ordered structures, such as nematic tactoids, membranes and their stacks, as well as twisted ribbons[37,40] are strongly favored. These depletion-driven self-assembled morphologies have been obtained using high molecular-weight depletants such as Dextran (molecular weight, M_w = 500 000 g mol^{-1}; radius of gyration, $R_g \sim 21$ nm), whose size is larger than the particle diameter. This results in the virus rods self-assembling into super-structures with predominant liquid-like or short-ranged positional order in at least two spatial directions.[37,40–42] However, in order to fully benefit from the morphology effect in terms of enhanced anisotropic properties of the resulting materials, highly ordered structures with crystalline, *i.e.* long-ranged positional order are required.[4,5,10]

In order to promote dense self-assembled structures with crystalline order short-ranged depletion attractions are required favoring small inter-rod distances, *s*. This effect can be achieved using a non-adsorbing polymer of small molecular weight (PEG, M_w = 8000 g mol^{-1}; $R_g \sim 4$ nm) added to a suspension of fd virus. The key-point here is that corresponding polymer coil has about the same size as the virus diameter, $2 \cdot R_g \sim d = 7$ nm. Taking advantage of the micrometer length of fd virus we are able to analyze the structures formed by these filamentous rods at the single particle scale using fluorescence optical microscopy.[39,43] We then investigate the detailed morphology of the virus-based superstructures upon varying both the depletion strength (osmotic stress tuned by polymer concentration) and rod volume fraction, while keeping the polymer size fixed thus ensuring the rod–rod interactions to be short-ranged.

Results and discussion

The experimental results are presented in Fig. 1. Here, we demonstrate that subtle morphological changes occur in a hierarchical way upon increasing the depletion strength. At low polymer concentration, when the depletion attraction is weak, the rods tend to aggregate side-by-side[44] thus minimizing their excluded volume. This results in the formation of 2D plate-shaped crystallites. These platelets have well-developed hexagonal facets (Fig. 1a) and are composed of a single layer of hexagonally packed aligned viral rods with a protruding needle-like defect located at the core.[43] The core-defect acts as a steric deterrent preventing the platelets to stack on top of each other.

Enhancing the depletion attraction causes an increase in the density number ρ_0 of plate-shaped nuclei and a simultaneous decrease of the platelet diameter (D = 1–2 μm) as well as a length reduction of the central core defect (Fig. 1b and Fig. S2, ESI†). This results in a decrease of the average platelet diameter D with increasing the depletion strength (Fig. S3, ESI†), since $\rho_0 \propto 1/D^2$ as dictated by particle mass conservation.

Upon increasing the depletion strength, the self-assembly process speeds up considerably resulting in much shorter typical growth times. Pushing the depletion strength even further we observe a high population of small platelets (of about $D \sim 1$ μm). Without a detectable central defect preventing their clustering, the small platelets begin to stack up and finally self-assemble into smectic-B like fibrils in which each layer represents a small hexagonal platelet with a width of about one rod length (Fig. 1c). This quasi-1D morphology referring to the overall resulting shape of the self-assembly can be interpreted as the result of fast-growing hexagonal platelets reversible polymerizing into smectic filaments. Clearly, the effective depletion attraction acting between platelets promotes face-to-face stacking in order to maximize the free volume available to the polymer.[29] In order to estimate the typical bond energy between monomeric platelets making up a smectic fibril, we invoke a simple reversible polymerization model described in detail in the ESI.† This theory assumes the length distribution of the smectic fibrils to result from a dynamical equilibrium between associating and dissociating plate monomers. At the low fibril concentrations probed in experiment, the fibrils are essentially non-interacting and their stationary length is chiefly determined by the reversible bonding of individual colloidal platelets undergoing Brownian motion. This reversible aggregation process is the central ingredient of this simple theoretical association model, which provides an analytical prediction of the fibril length distribution that can be compared to experimental results depicted in Fig. S4a (ESI†). From the exponential tails of the measured length distributions, we estimate a typical bonding energy between monomeric platelets of about 10 k_BT and a typical 'bonding volume' of effective range of attraction of about 8–10 times the polymer volume. The 'bonding volume' which can be interpreted as the bonding range times the platelet area is considerably less than the volume $\sim R^2 \cdot R_g$ with R the radius of a flat plate one would naively obtain from free-volume theory[29] if the face-to-face bonding was entirely due to ideal depletion attractions. Complicating factors such as thermal corrugation of the plate surface (due to fluctuations of the rods around their centers of mass), electrostatic interactions and semi-flexibility of the filamentous virus rods may account for the strongly reduced bond energy but these effects are notoriously difficult to capture within a simple, tractable model. The model also predicts the equilibrium constant of the fibril association and dissociation reactions to be quite large, suggesting fibril dissociation events to be much less frequent than bonding events, in particular for the longer fibrils. This finding is consistent with the fact that processes involving fibrils breaking up are difficult to observe experimentally, in particular at the low fibril concentrations explored here.

At the highest depletion attraction the growth kinetics speeds up dramatically resulting in the rods self-assembling into columnar bundles (Fig. 1d). In these structures, there is no layered organization along the main axis of the fiber but the hexagonal crystalline structure transverse to the bundle director n is preserved. The time required for the self-assembly processes, or growth time, is reduced dramatically when the growth morphology changes from the predominantly bidimensional platelets to the unidimensional fibers and bundles.

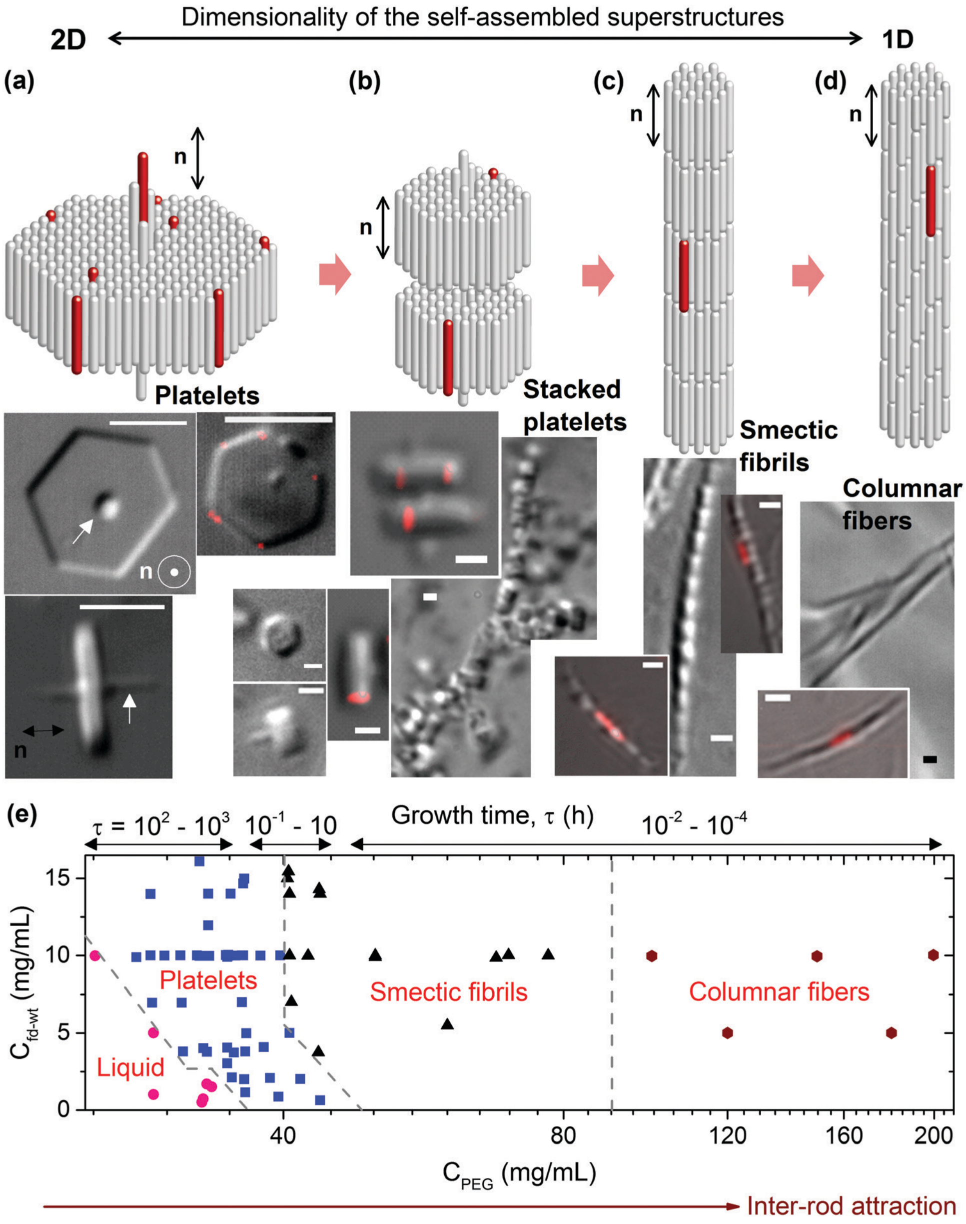

Fig. 1 Overview of morphological and dimensional changes in self-assembled structures formed by rod-like fd viruses driven by increasing depletion attraction. The kinetic processes determining the typical growth time for the various structures speeds up considerably with increasing inter-rod attraction. The self-assembled morphology changes from (a) hexagonal platelets composed of a one-rod thick monolayer of aligned fd rods with a central core defect (indicated by a white arrow), to (b) small hexagonal platelets and their stacks. When the attraction increases further, the rods self-assemble into (c) smectic-B like fibrils composed of small polymerized platelet monomers, and then to (d) columnar fibers. The fluorescently labeled viruses in the DIC/fluorescence overlaid images show that the rods are aligned parallel to the main axis n of the cluster (black double arrow). Scale bars, 5 μm for (a) and 1 μm for (b–d). (e) Phase diagram as a function of the rod ($C_{\mathrm{fd-wt}}$) and polymer (C_{PEG}) concentrations, where the typical growth time τ is also indicated. At each phase boundary, a gradual change of morphology occurs rather than a sharp transition.

Throughout the range of cluster morphologies observed, the typical growth time varies by more than six orders of magnitude, taking up days for large platelets to form, a few minutes for the smectic fibrils, down to milliseconds for the fast formation of columnar fibers. Apart from the intrinsic rod–rod attraction, kinetics play an important role in templating the self-assembled structures obtained. In view of the ultrafast growth process, we expect the formation of columnar bundles to be strongly marked by non-equilibrium effects, as columnar structures composed of long rods usually do not emerge from thermodynamic considerations.[29,45] In all the observed superstructures, the orientation of the rods (n) remains parallel to the main axis of the crystallite, as evidenced from the presence of a small fraction of virus rods labelled with a red fluorescent dye (Fig. 1) and using a full-wavelength retardation plate (Fig. S1, ESI†). The absence of any detectable particle self-diffusion within the clusters (Movies S1 to S5, ESI†) is consistent with the long-range positional order along the direction normal to

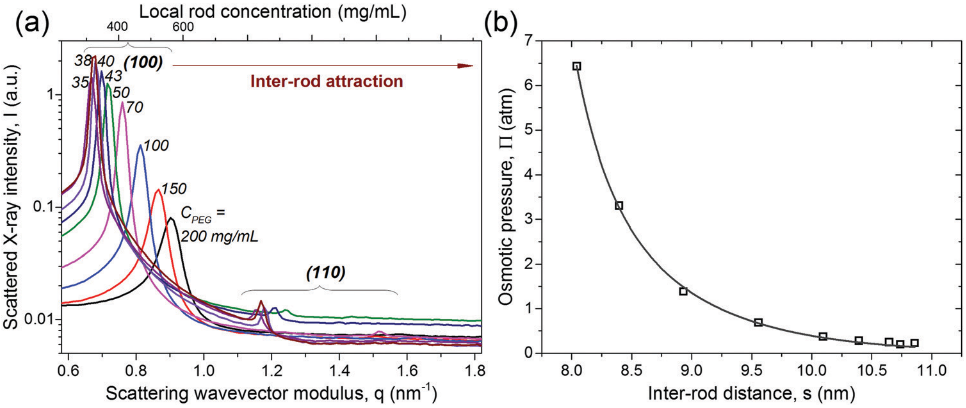

Fig. 2 SAXS data of the different virus-based self-assembled superstructures obtained by varying the concentration of PEG depletant (C_{PEG}). The initial virus concentration is set at 10 mg mL^{-1}. (a) SAXS spectra characteristic of hexagonal long-ranged positional order with the presence of sharp 100 and 110 Bragg reflections. The virus concentration within the self-assembled clusters, referred to as the local concentration, is calculated from the 2D swelling law associated with a hexagonal ordering of long rods[45] for a given (100) peak position. (b) Osmotic pressure (Π) obtained from the PEG concentration[46] as a function of inter-rod distance, $s = (4\pi/\sqrt{3})q_{100}{}^{-1}$. The fit (black curve) is based on the model of Yasar *et al.*[47] described in the ESI.†

n observed by small-angle X-ray scattering (SAXS) experiments (Fig. 2).

The SAXS experiments have been conducted at a fixed rod concentration but at varying polymer concentration and depletion strength. All SAXS spectra (Fig. 2a) display (100) and (110) diffraction peaks, characteristic of local hexagonal rod packing. The interaxial distance between the neighboring rods $s = (4\pi/\sqrt{3})q_{100}{}^{-1}$ can be directly obtained from the position of the main diffraction reflection. There is only little variation of the distance s (Fig. 2b) accompanying the vast morphological changes observed throughout the same range of conditions. Since the interaxial rod distance s probed by SAXS is about two orders of magnitude smaller compared to the rod length ℓ, a 2D swelling law ($q_{100} = \eta \cdot C_{\text{rod}}{}^{1/2}$) of the hexagonal lattice is expected, with $\eta = \left(8\pi^2 N_{\text{A}}\ell/\left(\sqrt{3}M_{\text{w}}\right)\right)^{0.5}$. From this, the local rod concentration associated with the various self-assembled morphologies can be deduced. This gives a value of around 300 mg mL^{-1} for the platelets, 350–400 mg mL^{-1} for the smectic fibrils, and 450–550 mg mL^{-1} for the columnar bundles (Fig. 2a).

The depletion interaction between the virus rods can be accounted for by invoking a polymer-generated osmotic pressure Π acting on the virus arrays. Here, one simply assumes that most of the polymer is excluded from the virus-based superstructures.[48] Such models, described in the ESI,† have been successfully applied to many charged rod-like particles,[47,49] and give an accurate description of the experimental data as shown in Fig. 2b.

Fig. 3 displays the crossover from one self-assembled superstructure to another in terms of the aspect ratio AR = h/D of the typical cluster morphology, with h and D indicating the height and diameter of the superstructure measured parallel and perpendicular to the rod director n, respectively. Throughout the range of attractions, the diameter decreases from 20–30 μm for the platelets while reaching a minimum of around 0.9 μm for the smectic fibers and columnar bundles (ESI,† Fig. S3 and S4). The height increases from one rod-length for single platelets to 10–20 μm for smectic fibers and columnar bundles (ESI,† Fig. S3 and S4). Consequently, the aspect ratio AR of the cluster morphology varies by almost three orders of magnitude throughout the probed range of depletion strengths. This demonstrates a high degree of shape-tunability of the self-assembled clusters, while guaranteeing the long-ranged positional order within the structures as demonstrated by the SAXS experiments.

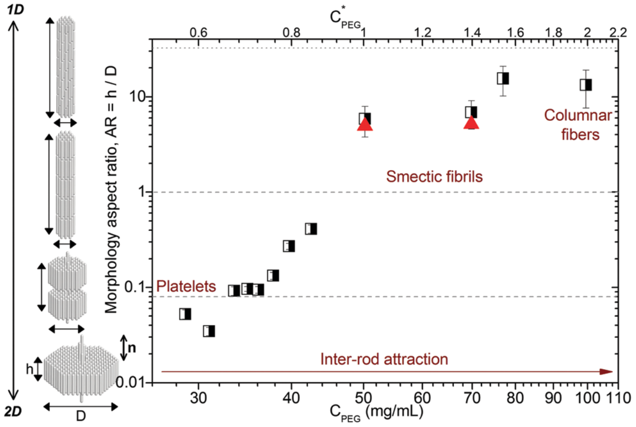

Fig. 3 Morphological transition from 2D to 1D self-assembled structures observed by enhancing the inter-rod attraction, in turn controlled by the strength of the depletion interaction. The cluster aspect ratio AR, defined as the dimension parallel to n (h; height) over the dimension perpendicular to n (D; diameter) where n denotes the main axis of the cluster morphology, is plotted (black and white squares) as a function of the depletant concentration. Experimentally, the largest measurable length is around 20 μm (the corresponding aspect ratio is indicated by a dotted line), since longer fibrils no longer lie within the same focal plan. The red triangular symbols represent the theoretical predictions from a simple reversible polymerization theory describing the formation of smectic fibrils (see ESI†), and they show a good quantitative agreement with experimental data. The typical bond energy between monomeric platelets within the smectic fibrils is estimated to be about 10 $k_{\text{B}}T$.

Films of highly aligned smectic fibers can be obtained upon applying weak shear flow, as shown in Fig. 4a. The degree of alignment can be established from a 2D nematic order parameter $S = \langle 2\cdot\cos^2(\theta) - 1\rangle$ that we can extract from the orientational

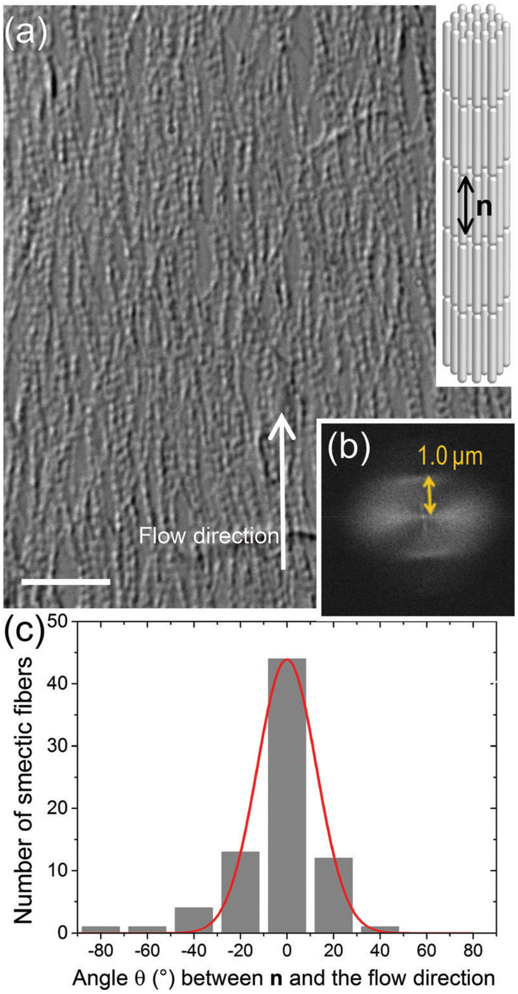

Fig. 4 Flow assisted alignment of smectic fibrils deposited on a glass substrate. (a) DIC image of the smectic fibrils, whose main axes (n) are along the flow direction. Scale bar, 10 μm. (b) Fourier transform pattern of the DIC image in (a), with the one-rod-thick smectic layer spacing indicated. (c) Distribution of smectic fibril orientations fitted by a Gaussian function (red line), from which the 2D orientational order parameter, $S = \langle 2\cdot\cos^2(\theta) - 1\rangle = 0.91$, can be obtained after numerical integration.

distribution of smectic fibrils (Fig. 4c). Typical values we found are of about $S = 0.90$ (note that $S = 1$ indicates perfect alignment, and $S = 0$ complete orientational disorder). This shows that these self-assembled superstructures are strongly susceptible to external orientation stimuli and can be readily shaped into macroscopically aligned domains. The facile processability of these rod-based superstructures opens perspectives for applications requiring anisotropic stimuli-responsive materials with internal crystalline order.[9,10,14,31,50]

Conclusion

In conclusion, we have described a tunable self-assembly process of rod-like particles forming superstructures with an unprecedented control of their cluster morphology, effective dimension and internal microstructure. In our system of filamentous fd virus rods mixed with PEG polymer, controlled self-assembly is achieved through the use of tunable short-ranged depletion interactions between the rods generated by the presence of non-adsorbing polymer with typical size comparable to the rod diameter. A systematic increase in the polymer concentration causes a number of morphological transitions affecting the principal dimensionality of the self-assembled structure. These range from isolated quasi-bidimensional platelets and stacked oligomeric platelets at weak depletion to unidimensional polymeric smectic fibrils, and columnar fibers at strong depletion. These polymorphological changes occur without compromising the long-ranged hexagonal crystal order within the superstructures. The average inter-rod distance is only weakly affected by the depletion strength. Simple thermodynamic considerations enable us to predict the typical fibril length and infer the typical bond energy between monomeric platelets within these structures. Last but not least, we have demonstrated the possibility of flow-assisted templating of such anisotropic superstructures into highly aligned supported films demonstrating a high degree of processability. By expanding the spectrum of bottom-up approaches towards anisotropic nanoparticles we argue that depletion-driven rod suspensions displaying hierarchically-tunable morphogenesis constitute a promising candidate for fabricating self-assembled structures for use in devices depending on anisotropic stimuli-responsive materials.

Materials and methods

Virus stock suspensions

Wild-type fd bacteriophages were grown with ER2738 strain of *E. coli* as host bacteria, and were purified according to standard protocols.[51] The fd–wt (wild type) viruses are rod-like particles, monodisperse in size and shape, with contour length ℓ = 880 nm and diameter d = 7 nm. In suspension, the virus rods have been shown to behave as near-hard rods exhibiting a well-defined liquid-crystalline phase behavior.[39–41,45] Virus suspensions were extensively dialyzed against TRIS–NaCl–HCl buffer (pH 8.2) at 110 mM of ionic strength, to ensure that the electrostatic repulsion between viral particles is strongly screened (Debye screening length, λ_D = 0.9 nm). The rods were subsequently concentrated using ultracentrifugation and redispersed at 30–35 mg mL^{-1} in the same buffer solution. The virus concentration was determined using spectrophotometry at the peak absorption wavelength of 269 nm with an optical density of 3.84 cm^2 mg^{-1}.[52] Fluorescently-labeled virus batches were separately prepared by conjugating Alexa Fluor 488-TFP ester (Invitrogen) or Dylight550-NHS ester (ThermoFischer) to their coat proteins. These labeled viruses were added in tracer amounts (0.001% (w/w) to 0.1% (w/w)) to the non-labeled virus batches for tracking by fluorescence microscopy.

Sample preparation

Polyethylene glycol (PEG) of M_w = 8000 g mol^{-1} (Sigma-Aldrich) was used as a non-absorbing polymer with a radius of gyration (R_g) of 4 nm in aqueous solution.[53] All polymer–virus mixtures were prepared in TRIS–NaCl–HCl buffer (pH 8.2) adjusted at

110 mM of ionic strength, and injected into optical microscopy cells. The cells were made by a glass slide and a coverslip (initially cleaned with sulfochromic acid) separated by a Mylar or Parafilm spacer, to obtain a cell thickness of about 100 μm. The cells were then sealed with UV-cured glue (NOA81, Epotecny). For the film of aligned smectic fibers, the samples were either prepared by drop casting on a cover slip, or loaded and oriented in the cell through capillary forces. Samples for small-angle X-ray scattering (SAXS) experiments were prepared in cylindrical quartz capillaries (diameter ∼ 1.5 mm; Mark–Röhrchen), filled with aqueous virus–polymer mixtures (∼20 μl for each), and sealed by flame. The capillaries were positioned vertically (gravity along the main axis of a capillary) for about 4 weeks in order to induce macroscopic phase separation through sedimentation of the self-assembled structures at the capillary bottom.

Optical microscopy

Differential interference contrast (DIC) and epifluorescence images were obtained using an inverted microscope (IX71, Olympus) equipped with an oil-immersion objective (NA 1.4, ×100 UPLSAPO), a mercury-halide excitation source (X-cite120Q, Excelitas), and a fluorescence imaging camera (NEO sCMOS, Andor Technology). To enable simultaneous acquisition of DIC and fluorescence images, an optical splitter setup (Optosplit II, Cairn Research) was used to divide each image into two channels thanks to a dichroic beamsplitter and band pass filters. The images obtained from both channels were then overlaid. The whole imaging system was operated by computer-interface software (Meta-Morph, Molecular Devices).

Small angle X-ray scattering (SAXS)

SAXS measurements were performed at the SWING beamline at the synchrotron facility SOLEIL (Orsay, France) operating at a source wavelength of $\lambda = 0.0995$ nm. The diffraction pattern was recorded by an AVIEX CCD detector, which was located in a vacuum detection tunnel with a sample-to-detector distance of 1.49 m. Angular integration was applied on the 2D SAXS pattern to obtain the scattering intensity as a function of scattering vector modulus, q.

Author contributions

B. S. prepared the samples, and performed the experiments. B. S. and E. G. analyzed the data. H. H. W. developed the theoretical polymerization model. E. G. conceived the project, designed experiments and fit the data. All authors wrote the manuscript.

Conflicts of interest

There are no conflicts to declare.

Acknowledgements

This work was supported by the French National Research Agency (ANR) through the project AURORE. We thank J. Perez from the SWING beamline for his kind assistance.

References

1 S. C. Glotzer and M. J. Solomon, Anisotropy of building blocks and their assembly into complex structures, *Nat. Mater.*, 2007, **6**, 557–562.

2 B. A. Grzybowski, C. E. Wilmer, J. Kim, K. P. Browne and K. J. M. Bishop, Self-assembly: from crystals to cells, *Soft Matter*, 2009, **5**, 1110–1128.

3 A. Stein, F. Li and N. R. Denny, Morphological control in colloidal crystal templating of inverse opals, hierarchical structures, and shaped particles, *Chem. Mater.*, 2008, **20**, 649–666.

4 W.-J. Chung, J.-W. Oh, K. Kwak, B. Y. Lee, J. Meyer, E. Wang, A. Hexemer and S.-W. Lee, Biomimetic self-templating supramolecular structures, *Nature*, 2011, **478**, 364–368.

5 T. Wang, J. Zhuang, J. Lynch, O. Chen, Z. Wang, X. Wang, D. LaMontagne, H. Wu, Z. Wang and Y. C. Cao, Self-assembled colloidal superparticles from nanorods, *Science*, 2012, **338**, 358–363.

6 J. H. Fendler, Chemical self-assembly for electronic applications, *Chem. Mater.*, 2001, **13**, 3196–3210.

7 B. A. Parviz, D. Ryan and G. M. Whitesides, Using self-assembly for the fabrication of nano-scale electronic and photonic devices, *IEEE Trans. Adv. Packag.*, 2003, **26**, 233–241.

8 S. S. Babu, H. Möhwald and T. Nakanishi, Recent progress in morphology control of supramolecular fullerene assemblies and its applications, *Chem. Soc. Rev.*, 2010, **39**, 4021–4035.

9 K. T. Nam, R. Wartena, P. J. Yoo, F. W. Liau, Y. J. Lee, Y.-M. Chiang, P. T. Hammond and A. M. Belcher, Stamped microbattery electrodes based on self-assembled M13 viruses, *Proc. Natl. Acad. Sci. U. S. A.*, 2008, **105**, 17227–17231.

10 B. Y. Lee, J. Zhang, C. Zueger, W.-J. Chung, S. Y. Yoo, E. Wang, J. Meyer, R. Ramesh and S.-W. Lee, Virus-based piezoelectric energy generation, *Nat. Nanotechnol.*, 2012, **7**, 351–356.

11 D. D. Lasic, D. Papahadjopoulos and R. Podgornik, in *Polymorphism of lipids, nucleic acids, and their interactions. Self-Assembling Complexes for Gene Delivery*, ed. A. V. Kabanov, P. L. Felgner and L. W. Seymour, Chichester: Wiley, 1998, pp. 3–26.

12 C. J. Drummond and C. Fong, Surfactant self-assembly objects as novel drug delivery vehicles, *Curr. Opin. Colloid Interface Sci.*, 2000, **4**, 449–456.

13 C. Sanchez, H. Arribart and M. M. Giraud Guille, Biomimetism and bioinspiration as tools for the design of innovative materials and systems, *Nat. Mater.*, 2005, **4**, 277–288.

14 A. Merzlyak, S. Indrakanti and S.-W. Lee, Genetically engineered nanofiber-like viruses for tissue regenerating materials, *Nano Lett.*, 2009, **9**, 846–852.

15 J. Zhang, Z. Sun and B. Yang, Self-assembly of photonic crystals from polymer colloids, *Curr. Opin. Colloid Interface Sci.*, 2009, **14**, 103–114.

16 W. Li, M. Döblinger, A. Vaneski, A. L. Rogach, F. Jäckel and J. Feldmann, Pyrite nanocrystals: shape-controlled synthesis and tunable optical properties via reversible self-assembly, *J. Mater. Chem.*, 2011, **21**, 17946–17952.

17 A. E. Saunders, A. Ghezelbash, D.-M. Smilgies, M. B. Sigman, Jr. and B. A. Korgel, Columnar self-assembly of colloidal nanodisks, *Nano Lett.*, 2006, **6**, 2959–2963.

18 W. A. Lopes and H. M. Jaeger, Hierarchical self-assembly of metal nanostructures on diblock copolymer scaffolds, *Nature*, 2001, **414**, 735–738.

19 Y. Lin, A. Böker, J. He, K. Sill, H. Xiang, C. Abetz, X. Li, J. Wang, T. Emrick, S. Long, Q. Wang, A. Balazs and T. P. Russel, Self-directed self-assembly of nanoparticle/copolymer mixtures, *Nature*, 2005, **434**, 55–59.

20 J. Fang, S. Du, S. Lebedkin, Z. Li, R. Kruk, M. Kappes and H. Hahn, Gold mesostructures with tailored surface topography and their self-assembly arrays for surface-enhanced Raman spectroscopy, *Nano Lett.*, 2010, **10**, 5006–5013.

21 K. Koziol, J. Vilatela, A. Moisala, M. Motta, P. Cunniff, M. Sennett and A. Windle, High-performance carbon nanotube fiber, *Science*, 2007, **318**, 1892–1895.

22 A. B. Dalton, S. Collins, E. Muñoz, J. M. Razal, V. H. Ebron, J. P. Ferraris, J. N. Coleman, B. G. Kim and R. H. Baughman, Super-tough carbon-nanotube fibres, *Nature*, 2003, **423**, 703.

23 J. Wang, R. P. Deo, P. Poulin and M. Mangey, Carbon nanotube fiber microelectrodes, *J. Am. Chem. Soc.*, 2003, **125**, 14706–14707.

24 X. Wang, C. J. Summers and Z. L. Wang, Large-scale hexagonal-patterned growth of aligned ZnO nanorods for nano-optoelectronics and nanosensor arrays, *Nano Lett.*, 2004, **4**, 423–426.

25 B. Peng, G. Li, D. Li, S. Dobson, Q. Zhang, J. Zhang, Y. H. Lee, H. V. Demir, X. Y. Ling and Q. Xiong, Vertically aligned gold nanorod monolayer on arbitrary substrates: self-assembly and femtomolar detection of food contaminants, *ACS Nano*, 2013, **7**, 5993–6000.

26 Y. Xie, Y. Li, G. Wei, Q. Liu, H. Mundoor, Z. Chen and I. Smalyukh, Liquid crystal self-assembly of upconversion nanorods enriched by depletion forces for mesostructured material preparation, *Nanoscale*, 2018, **10**, 4218–4227.

27 Y. Liang, Y. Xie, D. Chen, C. Guo, S. Hou, T. Wen, F. Yang, K. Deng, X. Wu, I. I. Smalyukh and Q. Liu, Symmetry control of nanorod superlattice driven by a governing force, *Nat. Commun.*, 2017, **8**, 1410.

28 S. Asakura and F. Oosawa, Interaction between particles suspended in solutions of macromolecules, *J. Polym. Sci.*, 1958, **33**, 183–192.

29 H. N. W. Lekkerkerker and R. Tuinier, *Colloids and the Depletion Interaction*, Springer, Dordrecht, 2011.

30 J. Zhang, P. R. Lang, W. Pyckhout-Hintzen and J. K. G. Dhont, Controllable synthesis and self-assembly of $PbCO_3$ nanorods in shape-dependent nonionic w/o microemulsions, *Soft Matter*, 2013, **9**, 7576–7582.

31 J. H. Lee, B. Fan, T. D. Samdin, D. A. Monteiro, M. S. Desai, O. Scheideler, H.-E. Jin, S. Kim and S.-W. Lee, Phage-based structural color sensors and their pattern recognition sensing system, *ACS Nano*, 2017, **11**, 3632–3641.

32 Y. Xie, S. Guo, Y. Ji, C. Guo, X. Liu, Z. Chen, X. Wu and Q. Liu, Self-assembly of gold nanorods into symmetric superlattices directed by OH-terminated hexa(ethylene glycol) alkanethiol, *Langmuir*, 2011, **27**, 11394–11400.

33 Y. Hata, T. Sawada and T. Serizawa, Macromolecular crowding for materials-directed controlled self-assembly, *J. Mater. Chem. B*, 2018, **6**, 6344–6359.

34 K. Zhao and T. G. Mason, Directing colloidal self-assembly through roughness-controlled depletion attractions, *Phys. Rev. Lett.*, 2007, **99**, 268301.

35 D. Baranov, A. Fiore, M. van Huis, C. Giannini, A. Falqui, U. Lafont, H. Zandbergen, M. Zanella, R. Cingolani and L. Manna, Assembly of colloidal semiconductor nanorods in solution by depletion attraction, *Nano Lett.*, 2010, **10**, 743–749.

36 K. L. Young, M. R. Jones, J. Zhang, R. J. Macfarlane, R. Esquivel-Sirvent, R. J. Nap, J. Wu, G. C. Schatz, B. Lee and C. A. Mirkin, Assembly of reconfigurable one-dimensional colloidal superlattices due to a synergy of fundamental nanoscale forces, *Proc. Natl. Acad. Sci. U. S. A.*, 2012, **109**, 2240–2245.

37 T. Gibaud, E. Barry, M. J. Zahkary, M. Henglin, A. Ward, Y. Yang, C. Berciu, R. Oldenbourg, M. F. Hagan, D. Nicastro, R. B. Meyer and Z. Dogic, Reconfigurable self-assembly through chiral control of interfacial tension, *Nature*, 2012, **481**, 348–351.

38 M. Adams and S. Fraden, Phase Behavior of Mixtures of Rods (Tobacco Mosaic Virus) and Spheres (Polyethylene Oxide, Bovine Serum Albumin), *Biophys. J.*, 1998, **74**, 669–677.

39 L. Saikia, T. Sarkar, M. Thomas, V. A. Raghunathan, A. Sain and P. Sharma, Curvature instability of chiral colloidal membranes on crystallization, *Nat. Commun.*, 2017, **8**, 1160.

40 Y. Yang, E. Barry, Z. Dogic and M. F. Hagan, Self-assembly of 2D membranes from mixtures of hard rods and depleting polymers, *Soft Matter*, 2012, **8**, 707–714.

41 Z. Dogic and S. Fraden, Development of model colloidal liquid crystals and the kinetics of the isotropic–smectic transition, *Philos. Trans. R. Soc., A*, 2001, **359**, 997–1015.

42 T. Gibaud, Filamentous phages as building blocks for reconfigurable and hierarchical self-assembly, *J. Phys.: Condens. Matter*, 2017, **29**, 493003.

43 B. Sung, A. de la Cotte and E. Grelet, Chirality-controlled crystallization via screw dislocations, *Nat. Commun.*, 2018, **9**, 1405.

44 M. P. B. van Bruggen and H. N. W. Lekkerkerker, Tunable attractions directing nonequilibrium states in dispersions of hard rods, *Macromolecules*, 2000, **33**, 5532–5535.

45 E. Grelet and R. Rana, From soft to hard rod behavior in liquid crystalline suspensions of sterically stabilized colloidal filamentous particles, *Soft Matter*, 2016, **12**, 4621–4627.

46 C. B. Stanley and H. H. Strey, Measuring osmotic pressure of poly(ethylene glycol) solutions by sedimentation equilibrium ultracentrifugation, *Macromolecules*, 2003, **36**, 6888–6893.

47 S. Yasar, R. Podgornik, J. Valle-Orero, M. R. Johmson and V. A. Parsegian, Continuity of states between the cholesteric → line hexatic transition and the condensation transition in DNA solutions, *Sci. Rep.*, 2014, **4**, 6877.

48 T. Gibaud and D. Constantin, Direct Liquid to Crystal Transition in a Quasi-Two-Dimensional Colloidal Membrane, *J. Phys. Chem. Lett.*, 2018, **9**, 4302–4307.

49 G. Abramov, R. Shaharabani, O. Morag, R. Avinery, A. Haimovich, I. Oz, R. Beck and A. Goldbourt, Structural Effects of Single Mutations in a Filamentous Viral Capsid Across Multiple Length Scales, *Biomacromolecules*, 2017, **18**, 2258–2266.

50 N. P. Reynolds, J. Adamcik, J. T. Berryman, S. Handschin, A. A. H. Zanjani, W. Li, K. Liu, A. Zhang and R. Mezzenga, Competition between crystal and fibril formation in molecular mutations of amyloidogenic peptides, *Nat. Commun.*, 2017, **8**, 1338.

51 J. Sambrook and D. W. Russell, *Molecular Cloning: A Laboratory Manual*, Cold Spring Harbor Laboratory Press, Harbor, NY, 3rd edn, 2001.

52 E. Barry, D. Beller and Z. Dogic, A model liquid crystalline system based on rodlike viruses with variable chirality and persistence length, *Soft Matter*, 2009, **5**, 2563–2570.

53 K. Devanand and J. C. Selser, Asymptotic behavior and long-range interactions in aqueous solutions of poly(ethylene oxide), *Macromolecules*, 1991, **24**, 5943–5947.

Electronic Supplementary Information
Depletion-driven morphological transitions in hexagonal crystallites of virus rods

Baeckkyoung Sung,[1] Henricus Herman Wensink,[2] and Eric Grelet[1,*]

[1]Centre de Recherche Paul-Pascal, UMR 5031,
CNRS & Université de Bordeaux, 33600 Pessac, France
[2] Laboratoire de Physique des Solides,
UMR 8502, CNRS & Université Paris-Sud,
Université Paris-Saclay, 91405 Orsay, France

---

[*] `grelet@crpp-bordeaux.cnrs.fr;eric.grelet@crpp.cnrs.fr`

I. SUPPLEMENTARY FIGURES

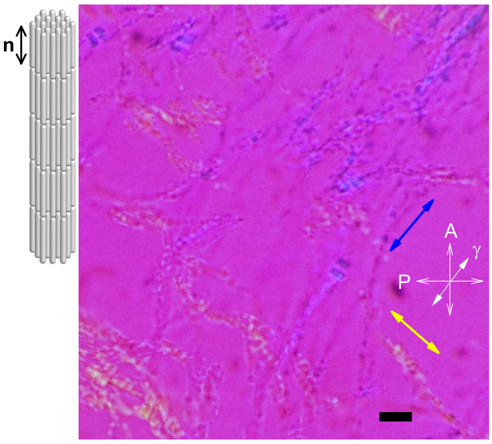

FIG. S1: Optical image of smectic fibers, where the sign of birefringence is verified with a full wavelength retardation plate, located between crossed polarizers (P and A). The retarded optical path results in fast (first order yellow) and slow (second order blue; marked by γ) axes in an isotropic medium (magenta background). The arrows represent the direction of the *fd* rods aligned parallel to the main axis (**n**) of the smectic fibers. Scale bar, 5 μm.

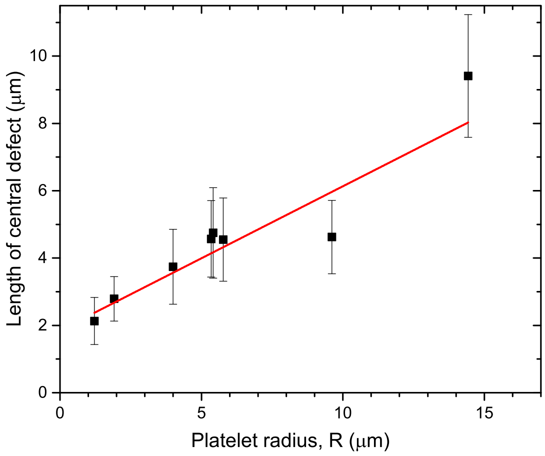

FIG. S2: Size of the central protruding defect as a function of the platelet diameter. A linear dependence is found, showing that the defect core reduces in size when the platelets become smaller. The smallest platelets show no discernible protrusions (defect length equal to platelet height) which enables them to stack on the top of each other forming smectic fibrils.

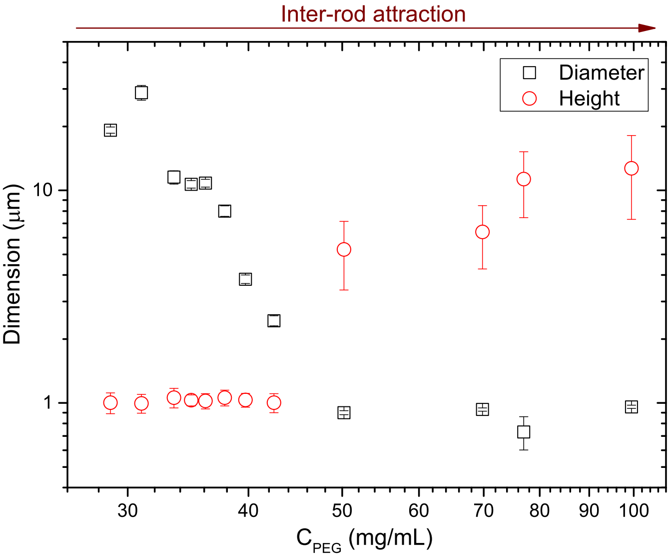

FIG. S3: Crossover from a 2D to 1D cluster morphology at increasing inter-rod attractions controlled by the PEG concentration (C_{PEG}) at a fixed rod concentration (C_{fd-wt} = 10 mg/mL). The variation of the cluster diameter (empty rectangles) and height (empty circles) enables a distinction between the different morphologies, as presented in Figure 3.

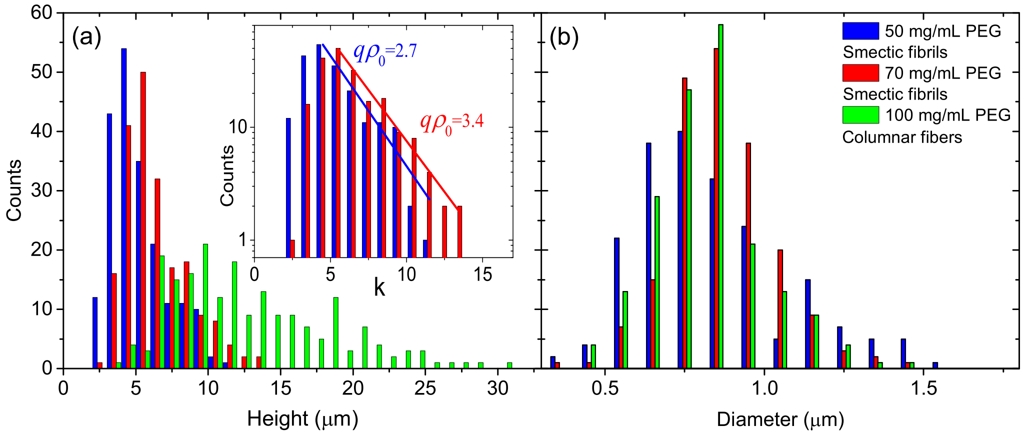

FIG. S4: Distributions of (a) heights, h, and (b) diameters, D, of the smectic fibrils (blue and red) and columnar bundles (green), for obtaining the mean values plotted in Figure S3. Inset: Log-lin representation of the smectic fibril degree of polymerization $k = h/\ell$, from which the fits (solid lines) using Eq. 16 provide $q\rho_0 = 2.7$ and 3.4 for C_{PEG} =50 and 70 mg/mL, respectively.

II. OSMOTIC PRESSURE FROM PEG SOLUTIONS (FIGURE 2B)

The osmotic pressure $\mathit{\Pi}$, in atm, is estimated according to the osmotic stress methods and is related to the PEG concentration C_{PEG}, in mg/mL, by using the following empirical relation [1]:

$$\mathit{\Pi} = -1.29G^2T + 127.6G^2 + 2.0G \tag{1}$$

with $G = C_{PEG}/(1000 - C_{PEG})$ and T the temperature, set at 22°C.

III. MODEL OF THE OSMOTIC PRESSURE APPLIED ON HEXAGONAL FD ARRAYS (FIGURE 2B)

In order to describe the osmotic pressure dependence of the charged viruses self-organized in a hexagonal lattice, a cylindrical cell model has been employed. In this model, a filamentous virus of bare radius $r = 3.5$ nm is surrounded by a cylindrical cell of diameter s, the interaxial rod distance, to account for the electric double layer. This yields a long-ranged electrostatic term $\mathit{\Pi}_e(s)$ of the the osmotic pressure, which is supplemented with a short-ranged repulsive hydratation contribution $\mathit{\Pi}_h(s)$. Both follow the same mathematical formulation and read up to leading order [2]:

$$\mathit{\Pi}(s) = \mathit{\Pi}_e(s) + \mathit{\Pi}_h(s) \tag{2}$$

where

$$\mathit{\Pi}_e(s) = A_e \left[K_0 \left(\frac{s}{2\lambda_D} \right) / K_1 \left(\frac{r}{\lambda_D} \right) \right]^2 \tag{3}$$

and

$$\mathit{\Pi}_h(s) = A_h \left[K_0 \left(\frac{s}{2\lambda_h} \right) / K_1 \left(\frac{r}{\lambda_h} \right) \right]^2 \tag{4}$$

Here $K_0(x)$ and $K_1(x)$ are the cylindrical modified Bessel functions of the second kind, and $\lambda_D = 0.9$ nm is the Debye screening length at ionic strength $I = 110$ mM. We fix the hydration repulsion length $\lambda_h = 0.25$ nm, according to the value found in literature [2, 3]. Upon fitting the data shown in Figure 2b, we obtain the values of both prefactors of Eqs. 3 and 4, $A_h \approx 175$ atm $\gg A_e \approx 175$ atm, which are consistent with those reported for DNA [2] and filamentous viruses [3].

IV. LINEAR REVERSIBLE POLYMERIZATION OF PLATELETS INTO SMECTIC FIBRILS

Let us consider a simple dynamical equilibrium whereby N_0 platelets (monomers) of thickness ℓ *reversibly* assemble into oligomers representing smectic fibrils of order $k = 1, 2, 3, ..., N_0$ and height $h = k\ell$. The formation and destruction of these k-mers is given by 'chemical reactions' described by:

$$kA_1 \underset{K_D}{\overset{K_A}{\rightleftharpoons}} A_k \tag{5}$$

where A_k denotes a $k-$mer of polymerization degree k, and K_A and K_D represent the association and dissociation rate constants, respectively. The rate of change of the $k-$mer concentration $[A_k]$ reads

$$\frac{d[A_k]}{dt} = K_A[A_1]^k - K_D[A_k] \tag{6}$$

Dynamic equilibrium $(d[A_k]/dt = 0)$ leads to the law of mass-action:

$$K_{eq} \equiv \frac{K_A}{K_D} = \frac{[A_k]}{[A_1]^k} \tag{7}$$

in terms of the equilibrium constant K_{eq}. The statistical physics of chain formation driven by simple attractive bonds between adjacent monomers has been analyzed in detail in References [4–6]. In the case of ideal *non-interacting* filaments, the law of mass-action translates into a steady-state distribution $\rho_k = [A_k]$ of $k-$mers (number of aggregates per unit volume) taking the following form:

$$\rho_k = \rho_1 (q\rho_1)^{k-1} \tag{8}$$

with ρ_1 the concentration of monomers, i.e. free unbonded platelets. The key parameter is the configuration integral q of a single depletion-driven bond which is defined as:

$$q \approx \exp(-\beta U_{\text{bond}}) \begin{cases} 0 & k_BT < U_{\text{bond}} \\ v_{ov} & k_BT > U_{\text{bond}} \end{cases} \tag{9}$$

Here, v_{ov} refers to the typical bonding volume which, assuming no other attractions than pure depletion, is expected to be of the order of the platelet surface times the depletion zone width R_g, i.e. $v_{ov} \sim R^2 R_g$. Within this simple picture we find a monomer-only regime when the thermal energy $k_BT > U_{\text{bond}}$ and $\rho_k/\rho_1 \downarrow 1$, whereas at low temperature $k_BT < U_{\text{bond}}$ a broad distribution of $k-$mers appears. From the thermal volume of a single bond q we can also determine the equilibrium constant of the reaction Eq. (5) via

$$K_{eq} \equiv \frac{K_A}{K_D} = (q\rho_0)^{k-1} \tag{10}$$

The normalization condition $\sum_{k=1}^{N_0} k\rho_k = \rho_0$ guarantees conservation of the total number of particles N_0 with ρ_0 the total monomer concentration. For $q\rho_1 < 1$ this leads to a closed expression for the aggregate distribution:

$$\rho_k = \frac{1}{q}\left(1 - \frac{2}{1+\sqrt{1+4q\rho_0}}\right)^k \tag{11}$$

From the average polymerization degree $\langle k \rangle$ we obtain the fibril aspect ratio (AR):

$$\text{AR} \sim \frac{\ell\langle k\rangle}{2R_m} = \frac{\ell}{2R_m}(1+\sqrt{1+4q\rho_0}) \tag{12}$$

with R_m the minimal plate radius.

V. EFFECTIVE BOND ENERGY FOR SMECTIC FIBRILS

Let us assume the formation of platelets to follow some kind of diffusion-limited aggregation (DLA) process which proceeds on a time-scale much shorter than the typical polymerization time of the monomeric platelets. We further assume that the platelets are all equal in size and have a radius R_m in which case the core defect protrusions that prevent the platelets from binding together have vanished (Figure S2). The total number density of platelets ρ_0 formed is dictated by the total number of rods N_r in the system, as conservation of mass requires that $\rho_r \propto \rho_0 R_m^2 \ell \rho_c$ with ρ_c the number density of rods within the crystalline platelet, and ρ_r the overall rod concentration. The number density of platelets then scales as $\rho_0 \propto \phi_r/\phi_c \ell R_m^2$ in terms of the corresponding overall ("r") and intraplatelet ("c") volume fractions $\phi_{r/c} \sim \rho_{r/c}\pi r^2 \ell$. The aggregate thermal volume Eq. (9) can then be expressed as follows:

$$q\rho_0 \sim \frac{\phi_r}{\phi_c}\frac{r}{\ell}e^{-U_{\text{bond}}/k_BT} \tag{13}$$

with $\phi_c \approx 0.5$ (corresponding to $C_{fd-wt} \approx 400$ mg/mL, see Figure 2a), $\phi_r \approx 0.01$ (corresponding to $C_{fd-wt} = 10$ mg/mL) and inverse rod aspect ratio $r/\ell \approx 0.04$. Here, we have tacitly assumed the bond energy U_{bond} to be larger than the thermal energy k_BT. The former is expected to increase with depletion strength and we conjecture:

$$\frac{U_{\text{bond}}}{k_BT} \sim -C^*_{\text{PEG}}\frac{v_{\text{bond}}}{v_{\text{pol}}} \tag{14}$$

in terms of the polymer (PEG) concentration $C^*_{\mathrm{PEG}} \sim P v_{\mathrm{pol}}$ renormalized to its overlap concentration. Here, $v_{\mathrm{pol}} \sim \frac{4\pi}{3} R_g^3$ represents the typical depletant volume. From Eq. (12),taking the monomer aspect ratio to be unity $\ell/2R_m \sim 1$ as experimentally observed, we infer that the fibril aspect ratio scales as:

$$\mathrm{AR} \sim 1 + \sqrt{1 + 4q\rho_0} \tag{15}$$

which enables a direct comparison with experimental data in Fig. 3. Values for $q\rho_0$ in the range from 2.7 to 3.4 can be extracted from the fibril length distribution ρ_k in Eq. (11) shown in Figure S4. To facilitate a fit with experimental data in the inset of Figure S4a, we recast the distribution Eq. (11) in exponential form, i.e.:

$$\rho_k \propto \exp\left(- \frac{2k}{1 + \sqrt{1 + 4q\rho_0}} \right) \tag{16}$$

which is justified for $q\rho_0 > 1$. We estimate the typical bonding energy between the polymerizing platelets in the smectic fibrils to be about $U_{\mathrm{bond}} \sim -10k_BT$ with the typical bonding volume between platelets lying in the range $v_{\mathrm{bond}} \sim 8 - 10v_{\mathrm{pol}}$. Recalling Eq. (10) we can estimate the ratio of the association and dissociation rate constants of the reaction Eq. (5), leading to $K_A/K_D \sim 3^{k-1}$. This suggests that for long filaments ($k \gg 1$) dissociation events are much less frequent than bonding events, which is consistent with experimental findings where fibril dissocation is not observed on the probed time scale.

VI. SUPPLEMENTARY MOVIES

The Supplementary Movies show time-stream DIC/fluorescence overlaid images acquired simultaneously (See Methods) to monitor the dynamics of red fluorescent labeled viruses trapped in the self-assembled structures (platelets, smectic fibrils, and columnar fibers) of non-labeled viruses.

Movies S1-S2. Small hexagonal platelets displayed as individual objects (Movie S1) and as face-to-face stacks (Movie S2), with edge-on view. In the platelets, the labeled single viruses are aligned along the main platelet axis and exhibit no discernible self-diffusion along or normal to the main rod direction. Brownian motion of the stacked platelets can be observed in Movie S2. Scale bar, 1 μm.

Movies S3-S4. Side-view of smectic fibers. A single labeled virus rod (Movie S3) and a labeled dimer virus (Movie S4) are incorporated within a single smectic-like layer (Movie S3) and in two adjacent smectic-like layers (Movie S4). These labeled viruses are aligned along the main cluster axis and do not show any self-diffusion along or normal to the rod direction. Scale bar, 1 μm.

Movie S5. Side-view of a columnar bundle. A labeled single virus is incorporated and aligns along the main axis of the bundle. This labeled virus does not show any self-diffusion along or normal to the main rod direction. Scale bar, 1 μm.

---

[1] C. B. Stanley and H. H. Strey, Measuring osmotic pressure of poly(ethylene glycol) solutions by sedimentation equilibrium ultracentrifugation, *Macromolecules*, 2003, **36**, 6888-6893.

[2] S. Yasar, R. Podgornik, J. Valle-Orero, M. R. Johmson and V. A. Parsegian, Continuity of states between the cholesteric-line hexatic transition and the condensation transition in DNA solutions, *Sci. Rep.*, 2014, **4**, 6877.

[3] G. Abramov, R. Shaharabani, O. Morag, R. Avinery, A. Haimovich, I. Oz, R. Beck and A. Goldbourt, Structural Effects of Single Mutations in a Filamentous Viral Capsid Across Multiple Length Scales, *Biomacromolecules*, 2017, **18**, 2258-2266.

[4] R. van Roij, Theory of Chain Association versus Liquid Condensation, *Phys. Rev. Lett.*, 1996, **76**, 3348.

[5] A. S. Perelson, F. W. Wiegel, The equilibrium size distribution of rouleaux, *Biophys J.*, 1982, **37**, 515-522.

[6] D. Frenkel and T. Schilling, Smectic filaments in colloidal suspensions of rods, *Phys. Rev. E*, 2002, **66**, 041606.